Nonlinear Discrete Mechanical Model of Steel Rings

Jibril Coulibaly, Marie-Aurélie Chanut, Stéphane Lambert, François Nicot

To cite this version:

Jibril Coulibaly, Marie-Aurélie Chanut, Stéphane Lambert, François Nicot. Nonlinear Discrete Mechanical Model of Steel Rings. Journal of Engineering Mechanics - ASCE, 2017, 143 (9), pp.04017087. 10.1061/(ASCE)EM.1943-7889.0001303 . hal-01987518

Nonlinear Discrete Mechanical Model of Steel Rings

Jibril B. Coulibaly[1]; Marie-Aurélie Chanut[2]; Stéphane Lambert[3]; and François Nicot[4]

Abstract: Circular rings are used in various engineering structures because of their nonlinear properties. The use of large assemblies of steel rings in flexible ring nets is widespread in recent technologies of protection structures and their design requires a nonlinear and computationally efficient mechanical modeling. This paper presents an innovative discrete model of steel rings for application in flexible protection structures. The model aims at providing an effective mechanical response of the net at both the local ring scale and the global net scale. Two different uniaxial tension configurations are defined as reference loading cases and the nonlinear analytical response of the ring model to these loading cases is established. A multicriteria numerical method based on the Levenberg-Marquardt algorithm is developed to calibrate the model param-eters from experimental data. An experimental campaign on steel wire spliced rings of different dimensions is conducted and permits the calibration and validation of the model.

Keywords: Steel rings; Mechanical model; Nonlinear; Numerical calibration method; Experimental campaign.

Introduction

Circular rings exhibit interesting nonlinear properties, making their usage advantageous for a wide range of engineering applications such as vibration and transient shock isolation (Hu and Zheng 2016) and protection structures (Lambert and Nicot 2011). Several approaches have been proposed to assess the behavior of circular rings. The nonlinear behavior of straight and curved beams was studied analytically and numerically by Seames and Conway (1957). Closed-form solutions, in terms of elliptic integrals, to the problem of elastic circular rings under uniaxial loading were proposed by Tse et al. (1994) and Tse and Lung (2000). This model shows good agreement with experimental data from tests performed on fiber-reinforced plastic composite rings. Numerical efforts to assess the response of such structures led to the development of various models of rings exhibiting relative advantages and drawbacks. Nicot et al. (2001b) proposed an analytical beam model using an approximation of the ring kinematics by two circular arcs. This model is well suited for steel rings because it also investigates plasticity and provides great insight into the combined geometrical-material nonlinearities of the ring. The finite-element method (FEM) was also used to model steel rings. Escallón et al. (2014) proposed a model using linear beam elements with a circular cross section. The number of beam elements used must be large and depends on the ring size. The elements are formulated with an elastoplastic constitutive behavior including strain-hardening and ductile damage evolution. It is able to capture finely the irreversible flexural bending of the ring, but requires section integration of a large number of elements, leading to a high computational cost.

This paper narrows the focus on steel rings used as elements of flexible structures. Protection structures against different types of hazards are often made of flexible netting surfaces intercepting incident projectiles. Projectiles can be diverse and range from cars or pipes blown away by tornadoes and capable of damaging industrial facilities, such as nuclear power plants, to falling rocks in mountainous areas, impacting roads, railroads, and houses (Lambert and Nicot 2011; EOTA 2013). Ring nets, made of a repeated pattern of interlaced steel rings, are widely used in recent designs of such protection structures. Upon impact, the net undergoes large dynamic deformations, leading to a change in its conformation due to rearrangements of its rings through yielding and relative sliding. Numerous technologies of steel rings exist, varying in the steel grade and wire strand assembly (clipped, spliced, welded). Hence, a general ring model must be technology-independent and adapt to various technological details of different rings. Models supporting dynamic and both geometrical and material nonlinear analyses are also necessary and, because a large amount of rings is to be assembled to form a net, computational efficiency is capital. In this regard, early theoretical developments presented in Seames and Conway (1957), Tse et al. (1994), and Tse and Lung (2000) are hardly suitable for such analyses. Likewise, practical use of fine FEM models such as Escallón et al. (2014) may suffer from their computational cost and the local information obtained from the discretization may be mostly underutilized for engineering applications. As a result, alternative methods have been proposed to efficiently determine ring nets behavior. Ghoussoub (2014) used homogenization of periodic media to treat the net as a membrane. This approach proved successful for infinitesimal strain and deflections but requires further improvements for large deflection applications. Homogenization techniques also lead to a loss of local information. A more common approach is the use of simplified discrete models of rings and ring nets. Nicot et al. (2001a) introduced a ring net model based on the discrete element method (DEM). Rings are discretized into a single node and the nodes are connected with bar elements of constitutive behavior modeling the ring response in uniaxial tension. Gentilini et al. (2012) also developed a similar model in FEM. Volkwein (2004) and Grassl (2002) respectively

---

[1] Ph.D. Student, Geological and Geotechnical Hazards Research Team, Cerema Centre-Est, 25 Ave. François Mitterrand, CS 92803, 69674 Bron Cedex, France (corresponding author). E-mail: jibril.coulibaly@cerema.fr; jibril.coulibaly@gmail.com

[2] Research Engineer, Geological and Geotechnical Hazards Research Team, Cerema Centre-Est, 25 Ave. François Mitterrand, CS 92803, 69674 Bron Cedex, France. E-mail: marie-aurelie.chanut@cerema.fr

[3] Research Engineer, UR ETGR, Université Grenoble Alpes, Irstea, Centre de Grenoble, 2 rue de la Papeterie-BP 76, F-38402 St-Martin-d'Hères, France. E-mail: stephane.lambert@irstea.fr

[4] Research Professor, UR ETGR, Université Grenoble Alpes, Irstea, Centre de Grenoble, 2 rue de la Papeterie-BP 76, F-38402 St-Martin-d'Hères, France. E-mail: francois.nicot@irstea.fr

developed 4-node and 8-node FEM models of steel rings and their corresponding net assemblies. These models proved more complete and efficient but present noticeable limitations such as their reversible behavior and unsuitability for different loading configurations. In this context, the need for an efficient nonlinear steel ring model accounting for most mechanical phenomena is left unfilled.

In this article, a new discrete model of steel rings is proposed. This technology-independent ring model takes into account the geometrical and material nonlinearities and uses a 4-node discretization with the aim of ensuring both a proper description of a single ring behavior and a computationally efficient modeling of large ring net assemblies. The general steel ring model is first presented. Analytical responses of the model to reference loading cases are then explored and a numerical fitting method is specifically developed to obtain the model optimal parameters. An experimental campaign is carried out and data are used to calibrate and validate the model against a given steel wire spliced ring technology used in rockfall restraining nets.

Ring Model

The mechanical behavior of steel rings under tension is first presented before introducing the proposed ring model. When external tensile forces are applied to a ring, combined bending and tension are undergone. Two regimes of deformation can be identified: an initial phase, termed *bending regime*, where bending is dominant and deflections are large, and a final phase, termed *tensile regime*, where tension is dominant and deflections are small (Nicot et al. 2001b; Escallón et al. 2014) (Fig. 1).

In the bending regime, the ring first deforms elastically until the onset of plastic strain. Deformation then continues with considerable changes in the ring shape due to plastic bending. As the ring deforms, its elastic stiffness increases as demonstrated by Tse and Lung (2000) for elastic rings. This result remains true for inelastic rings; the model proposed by Nicot et al. (2001b) accounting for plastic deformation shows a similar behavior. When going through cycles of loading and unloading, the larger the ring deformation, the stiffer the springback. This increase in the elastic stiffness of the ring structures is due to changes in its geometry. The unloading phases are elastic. When the ring is unloaded most of the tension vanishes, but because of its shape and elastoplastic behavior, residual elastic stresses due to bending remain present and the ring structure is autostressed. The stiffness of the ring structure remains moderate over the entire bending regime. When the ring is fully deformed, no extra bending forces can develop and the tensile regime starts. The ring mainly undergoes elastic tensile forces (Nicot et al. 2001b), and as a result its stiffness is very high. These features of steel rings behavior have also been illustrated by numerous experimental studies (Grassl et al. 2002).

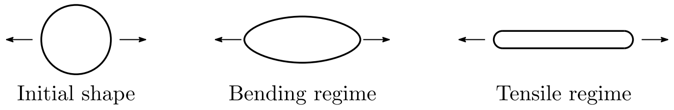

Fig. 1. Ring deformation and regime distinction

The developed ring model consists of four nodes interacting through an assembly of seven linkages: one perimeter linkage, two diagonal ones, and four side ones. For applications to rockfall restraining nets, the ring would be part of a 4-contact interlaced ring net in which each ring is attached to four other rings within the net [Fig. 2(a)]. The nodes would then represent the contact points of the ring with its surrounding counterparts [Fig. 2(b)] and form a minimal discretization of the ring structure that ensures computational efficiency; finer discretizations have been observed to be computationally more costly (Escallón et al. 2014; Volkwein 2004).

The role of each linkage is made explicit in the sequel. The perimeter linkage forms a closed loop like an actual ring, thus providing a correct geometric description of the curvature variations of a deformed ring (Tse and Lung 2000). This linkage produces tensile forces only as tension in an actual ring develops along its perimeter. Because of the chosen 4-node discretization, these forces represent the combined in-plane bending and tensile behavior of arcs of steel rings under tension. The diagonal and side linkages are referred to as internal linkages. They are different in nature but fulfill the same functions: they account for the in-plane plastic bending behavior of sections of the ring undergoing large curvature

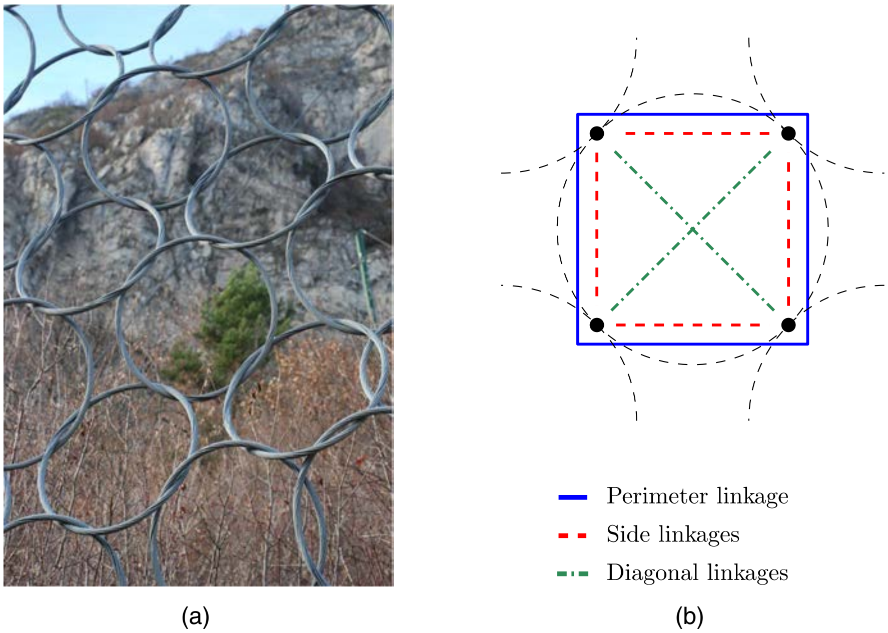

Fig. 2. (a) 4-contact ring net (image by Jibril Birante Coulibaly); (b) general 4-node ring model

variations and prevent the existence of zero-energy modes by balancing tensile forces from the perimeter with compression forces. The present developments only address in-plane bending of the ring. Although they remain limited, out-of-plane deformations might occur under certain loading cases and the model should exhibit some out-of-plane flexural rigidity. Assuming that the proposed model is bent about one of its diagonals, the other diagonal would shorten and develop a resisting force, providing the given model with out-of-plane flexural rigidity. Additional linkages could potentially be added to better account for this type of deformation. Such solutions are not investigated herein because of the limited effects out-of-plane deformations are expected to have compared with in-plane ones.

The combination of the seven linkages over the chosen discretization geometry enables modeling both the initial, low-stiffness, bending regime and the final, high-stiffness, tensile regime of the ring. The transition state separates the bending regime from the tensile regime; quantities at the transition state are written with an *r* in the subscript. The constitutive relations of the internal and perimeter linkages are now described in detail.

Internal Linkages Constitutive Relation

The diagonal and side linkages share the same type of constitutive relation. Internal linkages are given an elastoplastic constitutive relation. The constitutive relation of internal linkages accounts for the geometrical shape hardening of the ring structure demonstrated by Tse and Lung (2000). A one-dimensional (1D) elastoplastic constitutive relation is developed. The relation is first introduced in terms of the axial stress σ and the axial strain ε in the linkage. An equivalent and more convenient force–displacement relationship for use in the discrete model is derived subsequently. From strain partitioning, elastic strain ε^e and plastic strain ε^p are defined: $\varepsilon = \varepsilon^e + \varepsilon^p$. Stress is defined as $\sigma = E\varepsilon^e$. Let E be the current elastic modulus and E_0 be its initial value. The shape-hardening variable of the internal linkages G_{int} is defined as

$$G_{\text{int}} = \frac{E}{E_0} \geq 1 \tag{1}$$

Considering that changes in the ring shape are largely due to plastic bending, it is assumed that the elastic strain can be neglected in the hardening of the ring so that $G_{\text{int}} = g_{\text{int}}(\varepsilon^p)$ is an increasing function of the plastic strain only, with initial condition $g_{\text{int}}(\varepsilon^p = 0) = 1$. The onset of plastic strain does not occur instantly as the ring deforms (Nicot et al. 2001b; Escallón et al. 2014), so the shape-hardening function is therefore given the additional initial condition $dg_{\text{int}}/d\varepsilon^p(\varepsilon^p = 0) = 0$. The yield function is defined as $f(\sigma) = \sigma \leq 0$, along with the associated flow rule $\dot{\varepsilon}^p = \lambda \partial f/\partial\sigma$, where λ is the scalar plastic multiplier. The rate of deformation in the plastic domain is obtained through the Karush-Kuhn-Tucker conditions and the consistency condition. The stress-strain relationship is expressed as

$$\begin{array}{llll} \dot{\varepsilon} = \dot{\varepsilon}^e & \dot{\varepsilon}^p = 0 & \sigma = G_{\text{int}} E_0 \varepsilon^e \leq 0 & \text{for } f < 0 \\ \dot{\varepsilon} = \dot{\varepsilon}^p > 0 & \dot{\varepsilon}^e = 0 & \sigma = 0 & \text{for } f = 0 \text{ and } \dot{f} = 0 \end{array} \tag{2}$$

and the shape-hardening function g_{int} is taken as a power function

$$g_{\text{int}}(\varepsilon^p) = \begin{cases} 1 & \text{for } \varepsilon^p < \varepsilon^p_h \\ 1 + \alpha(\varepsilon^p - \varepsilon^p_h)^\beta & \text{for } \varepsilon^p > \varepsilon^p_h \end{cases} \tag{3}$$

with ε^p_h = largest plastic strain for which there is no hardening; and $\alpha > 0$ and $\beta > 1$ are coefficients to be determined.

A force–displacement formulation of the constitutive relation is now derived [Fig. 3(a)]. Considering a constant cross-section area A and initial unstretched length l_0, and using Cauchy strain, the linkage length l is given by $l = l_0(1 + \varepsilon)$. Eq. (2) shows that for a given level of plastic strain, the maximum length of the linkage is obtained when there is no elastic strain. Hence, the largest reached length l_i is also the current unstretched length and is given by $l_i = l_0(1 + \varepsilon^p)$. The elastic strain is then directly obtained from strain partitioning as $\varepsilon^e = (l - l_i)/l_0$. The force developed is $F = \sigma A$ and the yield surface may then be expressed as $f(F) = F \leq 0$. Introducing the initial stiffness of the linkage $k_0 = E_0 A/l_0$, the constitutive relation may be expressed in terms of force and displacement as

$$\begin{array}{llll} \Delta l \neq 0 & \Delta l_i = 0 & F = G_{\text{int}} k_0 (l - l_i) & \text{for } f < 0 \\ \Delta l > 0 & \Delta l_i = \Delta l & F = 0 & \text{for } f = 0 \text{ and } \dot{f} = 0 \end{array} \tag{4}$$

and the shape-hardening function g_{int} becomes

$$G_{\text{int}} = g_{\text{int}}(l_i) = \begin{cases} 1 & \text{for } l_i < l_{i_h} \\ 1 + a_{\text{int}}(l_i - l_{i_h})^{b_{\text{int}}} & \text{for } l_i > l_{i_h} \end{cases} \tag{5}$$

with l_{i_h} = largest length for which there is no hardening; and $a_{\text{int}} > 0$ and $b_{\text{int}} > 1$ = coefficients to be determined. The initial stiffness parameters and shape-hardening functions will respectively be noted as k_d and g_d for the diagonals and k_s and g_s for the sides. The largest length with no shape hardening and the shape-hardening

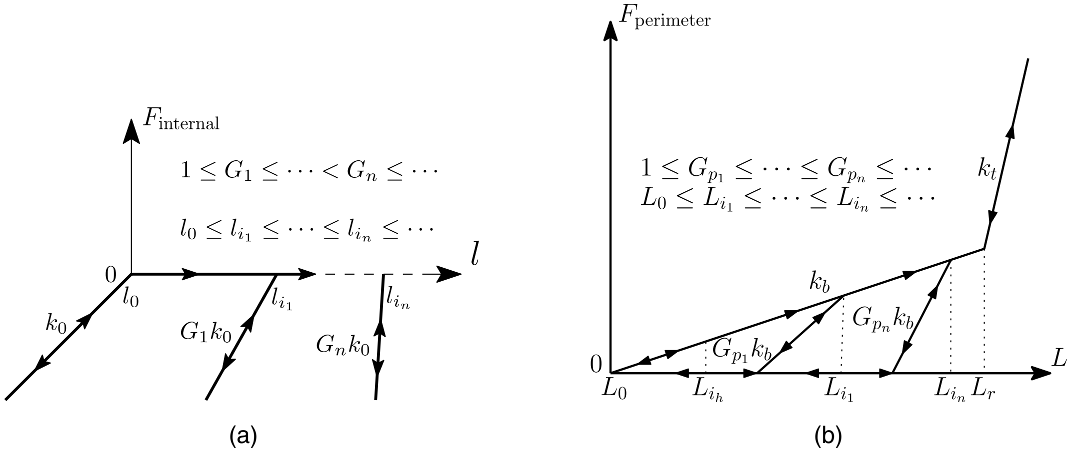

(a) (b)

Fig. 3. Constitutive relations of the (a) internal linkages; (b) perimeter linkage

parameters of both the diagonals and the sides will respectively be noted as d_{i_h}, a_d, b_d and s_{i_h}, a_s, b_s.

Perimeter Linkage Constitutive Relation

Similar to the internal linkages, the perimeter linkage is given an elastoplastic constitutive relation. The elastoplastic behavior of this linkage is inspired from the constitutive relation proposed by Nicot et al. (2001b) for a ring under uniaxial tension. The main properties are summed up hereafter and a simplified formulation is then derived [the detailed elastoplastic formulation can be found in Nicot et al. (2001b)]. The unstretched length of the perimeter linkage is noted as L_0, its current length as L, and its length at the transition state as L_r. First, for lengthening from $L = L_0$ up to $L = L_{i_h}$, the linkage response is elastic; this stage corresponds to the initial elastic bending of the ring with L_{i_h} being the largest perimeter length without plastic deformation. Second, for lengthening from $L = L_{i_h}$ up to $L = L_r$, the response is elastoplastic and corresponds to the combined tension and bending of the ring with large deflections in the bending regime. The linkage shows an irreversible behavior during this stage where the unloading path differs from the loading path and exhibits an increase in its stiffness with increased lengthening as explained previously. Third, for lengthening superior to the transition length $L = L_r$, the linkage shows an elastic response corresponding to the tensile regime of the ring. The stiffness of the linkage is very high during the tensile regime [Fig. 3(b)].

The monotonic force–displacement relationship of the perimeter linkage developed herein is defined as piecewise linear with stiffness coefficients k_b and $k_t > k_b$. The first piece, with stiffness parameter k_b, accounts for the low-stiffness, elastoplastic bending regime of the ring, while the second piece, with stiffness parameter k_t, accounts for the high-stiffness, elastic tensile regime of the ring. These linear pieces are separated at the transition length $L = L_r$ [Fig. 3(b)]. As for the internal linkages, a shape-hardening variable G_p is introduced in order to account for the increase in the elastic stiffness of the linkage k^e during the bending regime. This variable is defined as

$$G_p = \frac{k^e}{k_b} \geq 1 \tag{6}$$

The elastic stiffness depends almost solely on the plastic lengthening L^p so the shape-hardening variable of the perimeter linkage is a function of the plastic lengthening only, that is, $G_p = g_p(L^p)$. When loading monotonically in the bending regime, the linkage sustains elastic and plastic lengthening and exhibits tangent stiffness k_b. When unloading, it follows an elastic linear branch of tangent stiffness $k^e = G_p k_b$ until the force cancels; the reloading follows this same elastic branch up to the unloading point and takes back the monotonic path past this point [Fig. 3(b)]. The elastic stiffness in the tensile regime is k_t, therefore limiting the value of the shape-hardening variable to $G_p \leq k_t/k_b$.

Because the linkage deforms only in tension, the plastic lengthening cannot decrease and can only increase with an increase in the total length, that is, $\dot{L}^p = y(\dot{L}) \geq 0$, with y an increasing function. During the elastic phases, there is no increase in the plastic lengthening ($\dot{L}^p = 0$); the plastic lengthening can then only increase during the elastoplastic loading phases and may therefore be expressed in terms of the largest reached length L_i as $L_p = z(L_i)$, with z an increasing function. The plastic deformation could also be expressed in terms of the largest reached length for the internal linkages. The force–displacement relationship of the linkage and the evolution of the shape-hardening variable G_p may then be established in terms of the largest reached length L_i. The force–displacement relationship of the linkage is given by Eq. (7)

$$F = \begin{cases} k_b(L - L_0) & \text{for } L = L_i < L_r \text{ (loading)} \\ k_b(L_i - L_0) + G_p k_b(L - L_i) & \text{for } L < L_i < L_r \text{ (unloading)} \\ k_b(L_r - L_0) + k_t(L - L_r) & \text{for } L > L_r \end{cases} \tag{7}$$

The shape-hardening variable does not initially vary because plastic lengthening does not occur instantly as the ring deforms. When $L_i < L_{i_h}$, that is, $L^p = 0$, the linkage is elastic and $G_p = 1$; when $L_i > L_{i_h}$, that is, $L^p > 0$, the linkage underwent both elastic and plastic lengthening and $G_p > 1$. The shape-hardening variable $G_p = g_p(L_i)$ is therefore an increasing function of the largest reached length L_i with the following initial conditions: $g_p(L_i = L_0) = 1$ and $dg_p/dL_i(L_i = L_0) = 0$. The shape-hardening function g_p is also taken as a power function

$$G_p = g_p(L_i) = \begin{cases} 1 & \text{for } L_i < L_{i_h} \\ 1 + a_p(L_i - L_{i_h})^{b_p} & \text{for } L_r > L_i > L_{i_h} \end{cases} \tag{8}$$

with $a_p > 0$ and $b_p > 1$ = coefficients to be determined.

The analytical response of the model is investigated in the next section.

Analytical Response

As a structure, the ring mechanical response depends on the loading configuration and loading path. Two-point tensile tests are the most widely performed. Grassl et al. (2002) also mention results from various loading configurations, including 3-point and 4-point tensile tests. In the 4-contact net pattern, it is expected that the main loading configurations are 4-point and 2-point traction. Therefore, these configurations are considered as reference loading cases. The static, nonlinear, analytical response of the ring model under these two loading cases is explored hereafter.

4-Point Traction

The 4-point traction is performed as follows: an axial displacement δ is given to the top nodes, while the bottom nodes are fixed, and no lateral displacement is allowed [Fig. 4(a)]. The equilibrium equations of the top nodes are written on the deformed configuration [Fig. 4(b)]. Variable F_p is the tensile force in the perimeter linkage; F_d, F_{s_1}, and F_{s_2} are the compression forces in the diagonals, axial side, and transverse side linkages; the restraining force and R prevents lateral displacements so that the equilibrium [Eq. (9)] is always verified

$$\begin{aligned} F_p + F_{s_1} + F_d \sin\gamma - \frac{F}{2} &= 0 \\ F_p + F_{s_2} + F_d \cos\gamma - R &= 0 \end{aligned} \tag{9}$$

The monotonic loading and unloading are studied separately subsequently.

Monotonic Loading

During monotonic loading, internal linkages do not develop compression forces ($F_d = 0$, $F_{s_1} = 0$, and $F_{s_2} = 0$); the axial force F is given by Eq. (10), where δ_r is the axial displacement at the transition state

$$\begin{aligned} F &= 4k_b\delta & &\text{for } \delta < \delta_r \\ F &= 4k_b\delta_r + 4k_t(\delta - \delta_r) & &\text{for } \delta > \delta_r \end{aligned} \tag{10}$$

The force–displacement relationship is explicit and piecewise linear, similar to the perimeter one. The piecewise linear

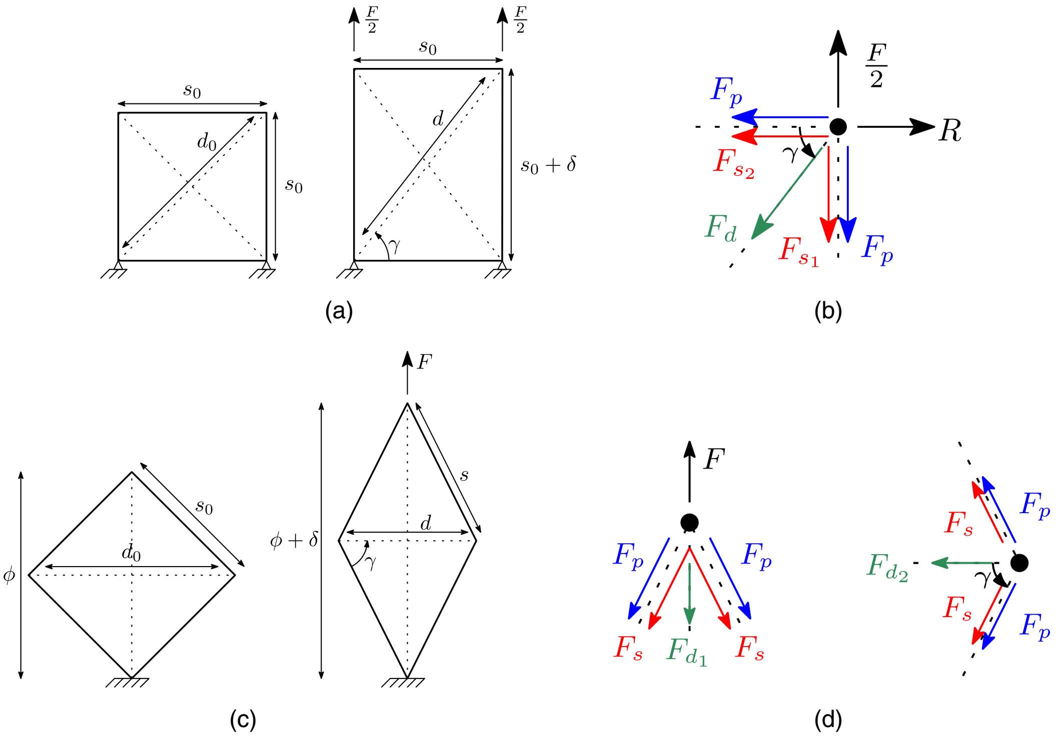

(a) (b)

(c) (d)

Fig. 4. Deformation kinematics and static equilibrium of the model: (a) 4-point traction kinematics; (b) 4-point traction equilibrium (top node); (c) 2-point traction kinematics; (d) 2-point traction equilibrium (top and sides nodes)

constitutive relation of the perimeter makes up for the lack of geometrical nonlinearities captured by the 4-node discretization.

Unloading

Considering a displacement δ_i was reached through monotonic loading, the direction of displacement is now reversed to unload the ring down to a displacement $\delta < \delta_i$. According to Eq. (4), the diagonals and the axial sides will start developing compression forces $F_d = G_{d_i} k_d (d - d_i)$, $F_{s_1} = G_{s_i} k_s (\delta - \delta_i)$, and $F_{s_2} = 0$ with $G_{d_i} = g_d(d_i)$ and $G_{s_i} = g_s(s_0 + \delta_i)$. According to Eq. (7), the expression of the tension in the perimeter changes in the bending regime for $\delta < \delta_r$. If unloading starts in the bending regime, that is, $\delta_i < \delta_r$, the tension in the perimeter is $F_p = 2k_b\delta_i + 2G_{p_i} k_b (\delta - \delta_i)$ and $G_{p_i} = g_p(4s_0 + 2\delta_i)$. If unloading starts in the tensile regime, that is, $\delta_i > \delta_r$, and continues in the bending regime ($\delta < \delta_r$), the tension in the perimeter is $F_p = 2k_b\delta_r + 2G_{p_r} k_b (\delta - \delta_r)$ and $G_{p_r} = g_p(4s_0 + 2\delta_r)$. The expression of the tension in the perimeter remains the same in the tensile regime for $\delta > \delta_r$. Accounting for these additional forces in the equilibrium Eq. (9), the force–displacement relationship becomes

$$\begin{aligned}
F &= 4k_b\delta_i + 4G_{p_i} k_b (\delta - \delta_i) + 2G_{s_i} k_s (\delta - \delta_i) \\
&\quad + 2G_{d_i} k_d (s_0 + \delta) \left(1 - \frac{d_i}{d}\right) \quad \text{for } \delta < \delta_i < \delta_r \\
F &= 4k_b\delta_r + 4G_{p_r} k_b (\delta - \delta_r) + 2G_{s_i} k_s (\delta - \delta_i) \\
&\quad + 2G_{d_i} k_d (s_0 + \delta) \left(1 - \frac{d_i}{d}\right) \quad \text{for } \delta < \delta_r < \delta_i \\
F &= 4k_b\delta_r + 4k_t (\delta - \delta_r) + 2G_{s_i} k_s (\delta - \delta_i) \\
&\quad + 2G_{d_i} k_d (s_0 + \delta) \left(1 - \frac{d_i}{d}\right) \quad \text{for } \delta_i > \delta > \delta_r
\end{aligned} \tag{11}$$

This relationship is demonstrated in Appendix I. The unloading path is unique. The equilibrium is also independent of the direction of loading, and as a result there is no hysteresis during unloading cycles. After reloading past δ_i, the response is not affected by the occurrence of an unloading cycle.

Eqs. (10) and (11) provide a general analytical response of the ring for any loading path in the 4-point traction configuration. Study of the 2-point traction configuration is carried out similarly to obtain the associated analytical response.

2-Point Traction

The 2-point traction is performed as follows: an axial displacement δ is given to the top node, the bottom node is fixed, and the side nodes are free [Fig. 4(c)]. In 2-point traction, the equilibrium equations of the top and side nodes are written on the deformed configuration [Fig. 4(d)]. As for the 4-point configuration, F_p is the tensile force in the perimeter linkage, and F_{d_1}, F_{d_2}, and F_s are the compression forces in the axial diagonal, transverse diagonal, and side linkages, respectively, so that the equilibrium of the top node and side nodes [Eq. (12)] are always verified

$$\begin{aligned}
2F_p \sin\gamma + 2F_s \sin\gamma + F_{d_1} - F &= 0 \,(\text{top node}) \\
2F_p \cos\gamma + 2F_s \cos\gamma + F_{d_2} &= 0 \,(\text{side nodes})
\end{aligned} \tag{12}$$

Because the side nodes are not fixed, there are two additional degrees of freedom: the ring diagonal length d and side length s. Taking advantage of the symmetries about the vertical and horizontal axes and using the Pythagorean trigonometric identity, the side length s is expressed in terms of the ring internal diameter ϕ, the axial displacement δ, and the transverse diagonal length d and nonlinear equations for the axial force F and transverse diagonal length d are derived. Similar to the 4-point traction, the monotonic loading and unloading phases are studied separately.

Monotonic Loading

During monotonic loading, the sides and the axial diagonal do not develop compression forces ($F_{d_1} = 0$ and $F_s = 0$). From the equilibrium Eq. (12), implicit relations are obtained for the two quantities F [Eq. (13)] and d [Eq. (14)], with s_r the side length at the transition state ($L_r = 4s_r$). These relationships are demonstrated in Appendix I

$$1 + \left[\frac{k_d\phi}{F + k_d(\phi+\delta)}\right]^2 - 32\left[\frac{k_b\phi}{4k_b(\phi+\delta) - F}\right]^2 = 0 \quad \text{for } s < s_r$$
$$1 + \left[\frac{k_d\phi}{F + k_d(\phi+\delta)}\right]^2 - 64\left[\frac{k_b(s_r - s_0) - k_t s_r}{F - 4k_t(\phi+\delta)}\right]^2 = 0 \quad \text{for } s > s_r \tag{13}$$

$$d = d_0\frac{k_d(\phi+\delta)}{F + k_d(\phi+\delta)} \quad \forall\ s \tag{14}$$

Unloading

Similar to the 4-point traction, the direction of displacement is reversed to unload the ring down to a displacement $\delta < \delta_i$ after δ_i was reached through monotonic loading. According to Eq. (4), the axial diagonal and all the sides will start developing compression forces $F_{d_1} = G_{d_i}k_d(\delta - \delta_i)$ and $F_s = G_{s_i}k_s(s - s_i)$ with $G_{d_i} = g_d(\phi + \delta_i)$ and $G_{s_i} = g_s(s_i)$. According to Eq. (7), the expression of the tension in the perimeter changes in the bending regime for $s < s_r$. If unloading starts in the bending regime, that is, $s_i < s_r$, the tension in the perimeter is $F_p = 4k_b(s_i - s_0) + 4G_{p_i}k_b(s - s_i)$ and $G_{p_i} = g_p(4s_i)$. If unloading starts in the tensile regime, that is, $s_i > s_r$, and continues in the bending regime ($s < s_r$), the tension in the perimeter is $F_p = 4k_b(s_r - s_0) + 4G_{p_r}k_b(s - s_r)$ and $G_{p_r} = g_p(4s_r)$. The expression of the tension in the perimeter remains the same in the tensile regime for $s > s_r$. These additional forces modify the equilibrium Eq. (12) and implicit expressions for the axial force F and the diagonal length d become

$$1 + \left[\frac{k_d\phi}{F - G_{d_i}k_d(\delta - \delta_i) + k_d(\phi+\delta)}\right]^2 - \left[\frac{8G_{p_i}k_b s_i + 2G_{s_i}k_s s_i - 8k_b(s_i - s_0)}{(4G_{p_i}k_b + G_{s_i}k_s)(\phi+\delta) + G_{d_i}k_d(\delta - \delta_i) - F}\right]^2 = 0 \quad \text{for } s < s_i < s_r$$
$$1 + \left[\frac{k_d\phi}{F - G_{d_i}k_d(\delta - \delta_i) + k_d(\phi+\delta)}\right]^2 - \left[\frac{8G_{p_r}k_b s_r + 2G_{s_i}k_s s_i - 8k_b(s_r - s_0)}{(4G_{p_r}k_b + G_{s_i}k_s)(\phi+\delta) + G_{d_i}k_d(\delta - \delta_i) - F}\right]^2 = 0 \quad \text{for } s < s_r < s_i$$
$$1 + \left[\frac{k_d\phi}{F - G_{d_i}k_d(\delta - \delta_i) + k_d(\phi+\delta)}\right]^2 - \left[\frac{8k_t s_r + 2G_{s_i}k_s s_i - 8k_b(s_r - s_0)}{(4k_t + G_{s_i}k_s)(\phi+\delta) + G_{d_i}k_d(\delta - \delta_i) - F}\right]^2 = 0 \quad \text{for } s_i > s > s_r \tag{15}$$

$$d = d_0\frac{k_d(\phi+\delta)}{F - G_{d_i}k_d(\delta - \delta_i) + k_d(\phi+\delta)} \quad \forall\ s \tag{16}$$

These relationships are demonstrated in Appendix I. As for the 4-point traction, the unloading path is unique with no hysteresis and the occurrence of an unloading cycle does not affect the response when reloading past δ_i.

The analytical response of the ring model to reference loading configurations is made fully explicit and all the parameters of the model are summarized in Table 1. The calibration method established to obtain the various model parameters from experimental data is presented in the next section.

Table 1. Parameters of the Ring Model

Parameter	Description	Unit
k_b	Initial perimeter stiffness in bending regime	N/m
k_t	Perimeter stiffness in tensile regime	N/m
k_d	Initial diagonal stiffness	N/m
k_s	Initial side stiffness	N/m
L_r	Perimeter transition length	m
L_{i_h}	Largest perimeter length with no shape hardening	m
d_{ih}	Largest diagonal length with no shape hardening	m
s_{ih}	Largest side length with no shape hardening	m
a_p	Perimeter shape-hardening function parameter a	—
a_d	Diagonal shape-hardening function parameter a	—
a_s	Side shape-hardening function parameter a	—
b_p	Perimeter shape-hardening function parameter b	—
b_d	Diagonal shape-hardening function parameter b	—
b_s	Side shape-hardening function parameter b	—

Model Calibration

The analytical response of the model depends on 14 parameters (Table 1) that need to be calibrated to fit existing technologies of rings. A numerical procedure has been developed in order to fit the analytical response to corresponding data.

Separation between the loading and unloading phases is essential. It is decided that the stiffness parameters and transition length of the perimeter must be obtained from the monotonic loading only while the shape-hardening functions are obtained thanks to the unloading cycles. The need for specific numerical fitting tools is justified by the piecewise, nonlinear, and implicit nature of the relations Eqs. (10), (11), and (13)–(16) to be fitted.

Finding the best set of parameters is done by means of the least-squares method. Consider m measurements of a given quantity X of the independent variable δ: the values of the experimentally measured quantity and the analytical quantity are respectively collected into vectors $\mathbf{X}_e$ and $\mathbf{X}_a$. The parameters of the analytical quantity are collected into the parameter vector $\boldsymbol{\theta}$. The least-squares method consists of finding the parameter set $\boldsymbol{\theta}$ minimizing the objective function

$$S(\boldsymbol{\theta}) = \sum_{j=1}^{m}[X_e(\delta_j) - X_a(\delta_j, \boldsymbol{\theta})]^2 = \|\mathbf{X}_e - \mathbf{X}_a(\boldsymbol{\theta})\|_2^2 \tag{17}$$

Optimal sets are noted $\boldsymbol{\theta}^*$ and the corresponding minimum value of the objective function is noted S^*. Given that the gradient of application S must be zero for it to be minimal, optimal sets are obtained solving Eq. (18) where $\mathbf{J}$ is the Jacobian matrix of the analytical quantity $\mathbf{X}_a$

$$\nabla S(\boldsymbol{\theta}^*) = -2\mathbf{J}^\top(\mathbf{X}_e - \mathbf{X}_a) = 0 \tag{18}$$

The developed numerical method aims at calibrating the transition length L_r along with stiffness parameters k_b, k_t, k_d, and k_s first, before calibrating the parameters of the shape hardening functions g_p, g_s, and g_d of the perimeter, side, and diagonal linkages. Because some parameters depend on others, calibration of the parameters in the given order is imperative.

Stiffness Parameters Calibration

For calibrating the stiffness parameters, the fit is performed on the monotonic loading of the 2-point traction because it provides more comprehensive data regarding the geometrical and material nonlinearities and possesses more degrees of freedom than the 4-point traction.

Minimization Problem

In order to satisfy the overall behavior of the ring, the force–displacement relationship, as well as the deformation kinematics, through the diagonal length d, are taken into account. To simplify the resolution, the transition length of the perimeter, through the side length s_r, is considered independent of $\boldsymbol{\theta}$ and varies in a chosen interval $[s_r^{\inf}; s_r^{\sup}]$ with a step Δs_r. The minimization problem is solved for all chosen values of s_r in the interval and the overall minimum value of the objective function is selected to obtain the optimal set of parameters $(s_r^*, \boldsymbol{\theta}^*)$. The parameter vector is $\boldsymbol{\theta} = (k_b, k_t, k_d)^\top$.

The objective functions to be minimized are

$$S_F(\boldsymbol{\theta}) = \|\mathbf{F}_e - \mathbf{F}_a(\boldsymbol{\theta})\|_2^2 \qquad S_d(\boldsymbol{\theta}) = \|\mathbf{d}_e - \mathbf{d}_a(\boldsymbol{\theta})\|_2^2 \tag{19}$$

The objective functions are not linear in terms of the parameter vector and are then minimized using the Levenberg-Marquardt (LM) nonlinear least-squares method (Marquardt 1963). The method consists of solving iteratively a quadratic minimization problem. At current iteration n, the analytical quantity is linearized $\mathbf{X}_a = \mathbf{X}_a^n + \mathbf{J}^n \Delta\boldsymbol{\theta}^n$ and a diagonal scaling term, using a damping factor $\lambda^n > 0$, is introduced. Eq. (18) becomes

$$[\mathbf{J}^{n\top}\mathbf{J}^n + \lambda^n \mathrm{diag}(\mathbf{J}^{n\top}\mathbf{J}^n)]\Delta\boldsymbol{\theta}^n = \mathbf{J}^{n\top}(\mathbf{X}_e - \mathbf{X}_a^n) \tag{20}$$

Updating the parameter vector $\boldsymbol{\theta}^{n+1} = \boldsymbol{\theta}^n + \Delta\boldsymbol{\theta}^n$ and solving iteratively, Eq. (20) converges to a minimum value for the objective function. Because nonquadratic problems may have several minimums, the resolution is performed for several starting points $\boldsymbol{\theta}^0$ that converge to different values of $\boldsymbol{\theta}^*$. The optimal set is found by taking the minimum value of all explored minimums.

Because it is unlikely that one set of optimal parameters minimizes both S_F and S_d, a unique solution to the multicriteria optimization problem of S_F and S_d must be found. The ideal point is defined in Ehrgott (2005) as the position in the objective space combining the optimal values of the objective functions taken separately, that is, $P^I = (S_F^*, S_d^*)$. The optimal parameter vector is found looking for the minimum distance D^I between the point $P(\boldsymbol{\theta}) = [S_F(\boldsymbol{\theta}), S_d(\boldsymbol{\theta})]$ and the ideal point. Because both functions are not homogeneous, the relative distance is used and 1-norm distance is used for simplicity. The distance to be minimized is therefore $D^I(\boldsymbol{\theta}) = \|[S_F(\boldsymbol{\theta}) - S_F^*]/S_F^*, [S_d(\boldsymbol{\theta}) - S_d^*]/S_d^*\|_1$. Minimizing distance D^I is equivalent to minimizing function S_{Fd} [Eq. (21)], hence, calibration of the stiffness parameters is performed minimizing the S_{Fd} function

$$S_{Fd}(\boldsymbol{\theta}) = \frac{S_F(\boldsymbol{\theta})}{S_F^*} + \frac{S_d(\boldsymbol{\theta})}{S_d^*} \tag{21}$$

Application of the LM algorithm to Eq. (21) is now presented.

Implementation

Minimizing S_{Fd} requires that minimization of Eq. (19) is first performed to obtain values of S_F^* and S_d^*. First, S_F^* is calculated. The values of the analytical axial force $\mathbf{F}_a$ are obtained solving the implicit force–displacement relationship in Eq. (13) using Brent's method (Brent 1973). The Jacobian matrix $\mathbf{J}_F$ of $\mathbf{F}_a$ is obtained analytically thanks to the implicit function theorem. Knowing $\mathbf{F}_a$ and $\mathbf{J}_F$, the optimal value S_F^* can be found using the LM algorithm [Eq. (20)]. Second, S_d^* is calculated. The values of the analytical diagonal length $\mathbf{d}_a$ are obtained from Eq. (14), involving the previously computed values of $\mathbf{F}_a$. The Jacobian matrix $\mathbf{J}_d$ of $\mathbf{d}_a$ is obtained by directly calculating its partial derivatives, which involve the previously computed partial derivatives of $\mathbf{F}_a$ because F is not an independent variable in the implicit expression Eq. (14). Knowing $\mathbf{d}_a$ and $\mathbf{J}_d$, the optimal value S_d^* can be found using the LM algorithm [Eq. (20)].

Once S_F^* and S_d^* are known, Eq. (21) can be minimized in the same manner. Taking advantage of the linearity properties, applying Eq. (20) to the multicriteria objective function S_{Fd} yields

$$\left[\frac{\mathbf{J}_F^\top \mathbf{J}_F}{S_F^*} + \frac{\mathbf{J}_d^\top \mathbf{J}_d}{S_d^*} + \lambda \mathrm{diag}\left(\frac{\mathbf{J}_F^\top \mathbf{J}_F}{S_F^*} + \frac{\mathbf{J}_d^\top \mathbf{J}_d}{S_d^*}\right)\right]\Delta\boldsymbol{\theta} = \frac{\mathbf{J}_F^\top(\mathbf{F}_e - \mathbf{F}_a)}{S_F^*} + \frac{\mathbf{J}_d^\top(\mathbf{d}_e - \mathbf{d}_a)}{S_d^*} \tag{22}$$

which gives the optimal set $\boldsymbol{\theta}^* = (k_b^*, k_t^*, k_d^*)^\top$. The set of optimal values $(s_r^*, k_b^*, k_t^*, k_d^*)$ is obtained but no optimal value of k_s is found yet. Because the side stiffness k_s does not appear in the monotonic loading equations, an extra configuration is used to find a value of k_s^* from loading equations only. The optimal value of the side stiffness parameter is given by Eq. (23), where δ_r^{2P} denotes the axial displacement at the transition state in 2-point traction [Fig. 4(c)]. This relationship is demonstrated in Appendix II

$$k_s^* = 2k_b^*\left(\frac{\phi - s_0 + \delta_r^{2P*}}{\phi + s_0 + \delta_r^{2P*} - 2s_r^*} - 1\right) \tag{23}$$

In the following, the procedure applied to calibrate the parameters of the shape-hardening functions is presented.

Shape-Hardening Functions Parameters Calibration

During 2-point traction, the extension of the diagonals is large, while the extension of the sides remains moderate [Fig. 4(c)]. Conversely, in 4-point traction, the extension of the diagonals is very limited and the sides undergo larger extension [Fig. 4(a)]. Therefore, the parameters of the shape-hardening functions of the sides and of the diagonals are calibrated independently: the 4-point traction is used to fit the parameters of the shape-hardening function of the sides, while the 2-point traction is used to fit the ones of the diagonals. The extension of the perimeter is comparable in 2-point and 4-point traction so that calibration of the perimeter shape-hardening function parameters could be performed on both configurations. The 4-point traction is used to fit the parameters of the shape-hardening function of the perimeter together with the shape-hardening parameters of the side for reasons explained in the upcoming paragraphs. The fit is performed on the unloading cycles only. As discussed previously, calibration order is important and the parameters of the shape-hardening function of the perimeter and of the sides must be calibrated prior to calibrating the parameters of the shape-hardening function of the diagonals to allow for independent calibration. Calibration of the parameters of functions g_p, g_s, and g_d is successively presented hereafter.

Perimeter and Side Shape-Hardening Functions

Volkwein (2004) reports experimental data from Grassl (2002) showing that in 4-point traction, the ultimate axial displacement is approximately 15% of the ring internal diameter. It has also been shown in Escallón et al. (2014) and Nicot et al. (2001a) that in 2-point traction, deformation remains elastic for axial displacement up to approximately 15% of the diameter. These results indicate that for the model to replicate this behavior, the diagonal linkages must not exhibit an increase in their stiffness for an extension up to approximately 15% of the ring internal diameter, meaning that in 4-point traction, failure would occur before the stiffness of the diagonal linkages starts to increase. As a consequence, the value of the shape-hardening function of the diagonals g_d is assumed to remain equal to 1 over the entire range of deformation of the 4-point traction and the model response only involves the variations of the shape-hardening function of the perimeter g_p and the sides g_s.

The force–displacement relationship in Eq. (11) for the unloading cycles in 4-point traction reveals that the shape-hardening variables of the perimeter G_p and of the sides G_s both have a strictly identical influence on the model response that depends linearly on these two parameters in the bending regime. As a result, there are an infinite number of pairs of shape-hardening parameters (G_p, G_s) that yield the same force–displacement response and there is no unique solution to the least-squares minimization problem. Implicit Eq. (15) for the unloading cycles in 2-point traction also shows an identical influence of the values of the shape-hardening variables of the perimeter and the sides, implying nonuniqueness of the solution sought.

To resolve this issue, the values of the shape-hardening variables are determined so as to minimize the elastic potential energy in the perimeter linkage. As presented in "Ring Model," when the ring is unloaded, tension vanishes and the ring structure reaches an autostressed configuration with balanced bending forces only. Similarly, when the model is unloaded, the elastic potential energy is redistributed from the perimeter to the internal linkages and the ring model finds an autostressed equilibrium configuration. Because the perimeter linkage bears the information regarding the tension in the ring, minimizing its potential energy enables adjusting the level of tension forces, as observed in actual rings. For a given unloading displacement, if the stiffness of the side linkages is high, the perimeter must apply a large tension to balance the compression forces developed by the sides. Little energy is then transferred to the side linkages and the elastic potential energy of the perimeter remains high. Conversely, if the stiffness of the side linkages is low, the balancing tension force applied by the perimeter must also be low. A larger amount of energy is then transferred to the side linkages and the elastic potential energy of the perimeter decreases. In order to minimize the elastic potential energy in the perimeter linkage, the stiffness of the side linkages must always remain as low as possible. As a consequence, it is considered that the side linkages do not sustain any shape hardening and that the value of the shape-hardening function of the sides g_s remains equal to 1.

The only varying parameter is the shape-hardening variable of the perimeter. The parameter vector is then $\boldsymbol{\theta} = G_{p_i}$. The least-squares fit is direct and has a unique solution because Eq. (11) is affine in $\boldsymbol{\theta}$. For every unloading cycle (i), Eq. (18) is solved for the axial force F from Eq. (11). Once values of G_{p_i} are obtained for various displacement values δ_i, the g_p power function is fitted to obtain parameters a_p, b_p, and L_{i_h}. The length L_{i_h} is taken as the largest length for which all computed values of G_{p_i} remain equal to 1.

Diagonal Shape-Hardening Function

Once the shape-hardening function of the perimeter g_p is known, the model response only depends on the variations of the shape-hardening function of the diagonals g_d. From Eq. (16) and using the implicit function theorem, it is demonstrated that the diagonal length d is independent of the stiffness value of the axial diagonal $G_d k_d$. Hence, the axial force F alone is fitted against the unloading cycles of the 2-point traction. The objective function S_F is then minimized for the parameter vector $\boldsymbol{\theta} = G_{d_i}$ using the LM algorithm. Once values of G_{d_i} are obtained for different displacement values δ_i, the g_d function is fitted the same way as g_p.

The numerical method to calibrate the model parameters is applied to experimental data in the next section.

Experiments and Results

In this section, the efficiency of the analytical model and calibration method are tested against experimental data. The general testing protocol providing the necessary input data for the model to be calibrated is also presented.

Experimental Campaign

Implementation and numerical simulations require every parameter of the model to be calibrated. The experimental protocol is defined so that the necessary and sufficient data can be obtained from testings of any given technology of rings. This protocol consists of applying the reference loading cases, i.e., quasi-static 2-point and 4-point traction, and recording the axial force, axial displacement, and diagonal length.

Setup

The test specimens are isolated rings of given internal diameter ϕ and strand diameter ϕ_t. The specimen is mounted in a specifically designed frame that allows modular 2-point and 4-point traction configurations (Fig. 5). The frame is made out of two heads, a fixed one and a mobile one in which connecting elements may be inserted and adjusted to fit the loading case and the ring internal diameter. The mobile head slides on a horizontal steel beam and is supported by polytetrafluoroethylene (PTFE) pads to ensure low friction. To replicate the ring contact with similar rings in the net, connecting elements of the same diameter as the ring strand diameter must be used. A displacement sensor measures the axial displacement δ of the mobile head, while a force sensor measures the axial force F; both sensors acquire data with a sampling frequency of 5,000 Hz. A Nikon (Tokyo, Japan) D600 digital single-lens reflex (DSLR) camera with an 85-mm focal length lens is placed approximately 3 m vertically above the testing unit to capture 6,016 × 4,016 pixel images of the planar deformation of the ring. Images are taken every half-second; the diagonal length d is obtained through image-processing with software

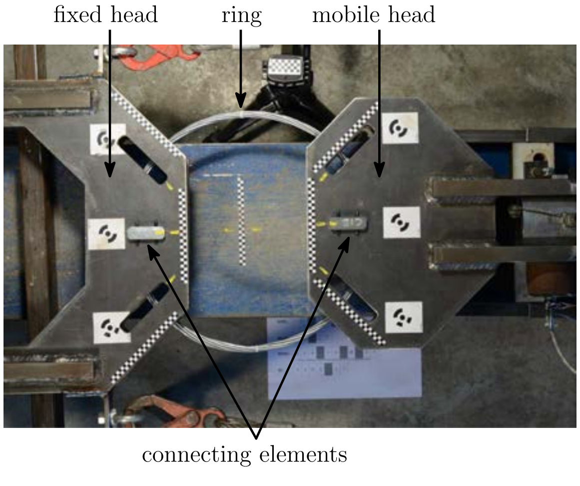

Fig. 5. Initial setup of a 2-point traction test with a ring mounted in the testing frame (image by Jibril Birante Coulibaly)

Table 2. Geometry of the Tested Rings

Group	Internal diameter ϕ (average) (mm)	Strand diameter ϕ_t (mm)
350/09	354	9
350/12	361	12
420/16	425	16

ImageJ version 1.48 (Schneider et al. 2012). The ring is deformed at a constant speed of 120 mm/min, as proposed in ETAG 27 (EOTA 2013), through loading and unloading cycles as all the data are acquired.

Experiments

An experimental campaign is carried out on three groups of steel wire spliced rings. The main characteristics of the tested rings are presented in Table 2. Preliminary design of the rings has been performed by the manufacturer in accordance with ultimate strength requirements. The adequate determination of the ring dimensions is not of interest in the present method.

For every group, five rings are tested (numbered 01–05) in 2-point (2P) and 4-point (4P) traction. For every test, four cycles of loading-unloading are performed at constant speed. A total of 30 tests are performed to calibrate and validate the present model.

Results

Experimental data and calibration results are presented in this section. For clarity and concision, comprehensive results are reported for the 350/12 rings before reporting the essential results for the 350/09 and 420/16 rings.

Experimental Observations

The experimental force–displacement relationships in 4-point traction [Fig. 6(a)] and 2-point traction [Fig. 6(b)] are presented and compared with the existing models and experimental data available in the literature. The force range in Figs. 6(a and b) is chosen so that unloading cycles appear distinctively. To begin with, the curves show consistency in the rings' response and little variability that can be attributed to the variations in the ring diameter. Smaller rings exhibit smaller displacements for a given force, resulting in an overall higher stiffness during both loading and unloading phases. In addition, the low-stiffness bending regime and high-stiffness tensile regime are observed in the data, illustrating Nicot et al.'s (2001b) observations and regime distinction and confirming that the hardening spring behavior demonstrated by Tse and Lung (2000) for axially tensioned elastic rings is also valid for elastoplastic rings. Initial stiffness in the bending regime is higher in the 4-point traction than in the 2-point traction, while both show comparable stiffness in the tensile regime as reported by Volkwein (2004) presenting experimental data from Grassl (2002). Eventually, irreversibility of the deformation and increase in the stiffness of the springback as reported by Nicot et al. (2001b) are also observed in the data. Unloading cycles differ from the loading path, showing a dissipation of energy due to plastic bending. The cycles also present some hysteresis; it is, however, difficult to assess whether it comes from an irreversible process occurring in the ring itself or in the testing apparatus, namely, friction and backlash between the parts of the setup. The stiffness of the unloading cycles is rather constant within a given cycle and increases as the axial displacement increases, showing that the shape hardening can be mostly attributed to plastic deformation as it is assumed in the proposed model.

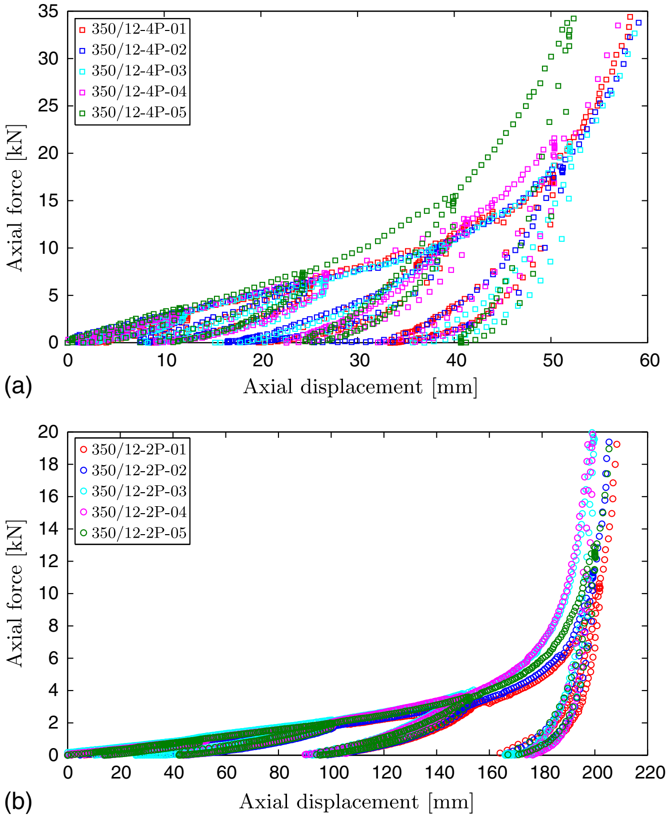

Fig. 6. Experimental force–displacement curves for 350/12 rings: (a) 4-point traction; (b) 2-point traction

Model Response

The calibration method previously presented is applied to obtain the best-fit parameters for the tested rings. Calibration results are presented for monotonic loading first and then unloading cycles so as to follow the logical order of the calibration process.

The optimal value of the transition length L_r and stiffness parameters k_b, k_t, k_d, and k_s are calibrated from the monotonic loading data in 2-point traction, and results on the overall response of the ring show good accordance [Figs. 7(a and b)]. The choice of the multicriteria method is supported by the agreement of the fit on both the axial force F and the diagonal length d. The nonlinearities as well as the bending and tensile regimes are both properly captured by the discrete model, demonstrating its suitability for steel ring modeling.

The model is validated by comparing its monotonic response in 4-point traction with the corresponding experimental data. As a matter of fact, calibration for monotonic loading is made solely using data from the 2-point traction configuration, hence, the 4-point traction response of the model is independent of the experimental data in this very configuration. Comparison of the model response and experimental data shows satisfying accordance [Fig. 7(c)] and demonstrates the capacity of the model to account for various loading configurations. The stiffness parameters are slightly underestimated in the bending regime and overestimated in the tensile regime. The affine response of the model is due to the 4-node discretization. The model, like actual rings, exhibits a higher stiffness in 4-point traction than in 2-point traction in the bending regime and identical stiffness for both configurations in the tensile regime [Fig. 7(d)]. Other models, such as the discrete 8-node model proposed by Grassl (2002) and the FEM beam model proposed by Escallón et al. (2014), also present limitations in fitting the response

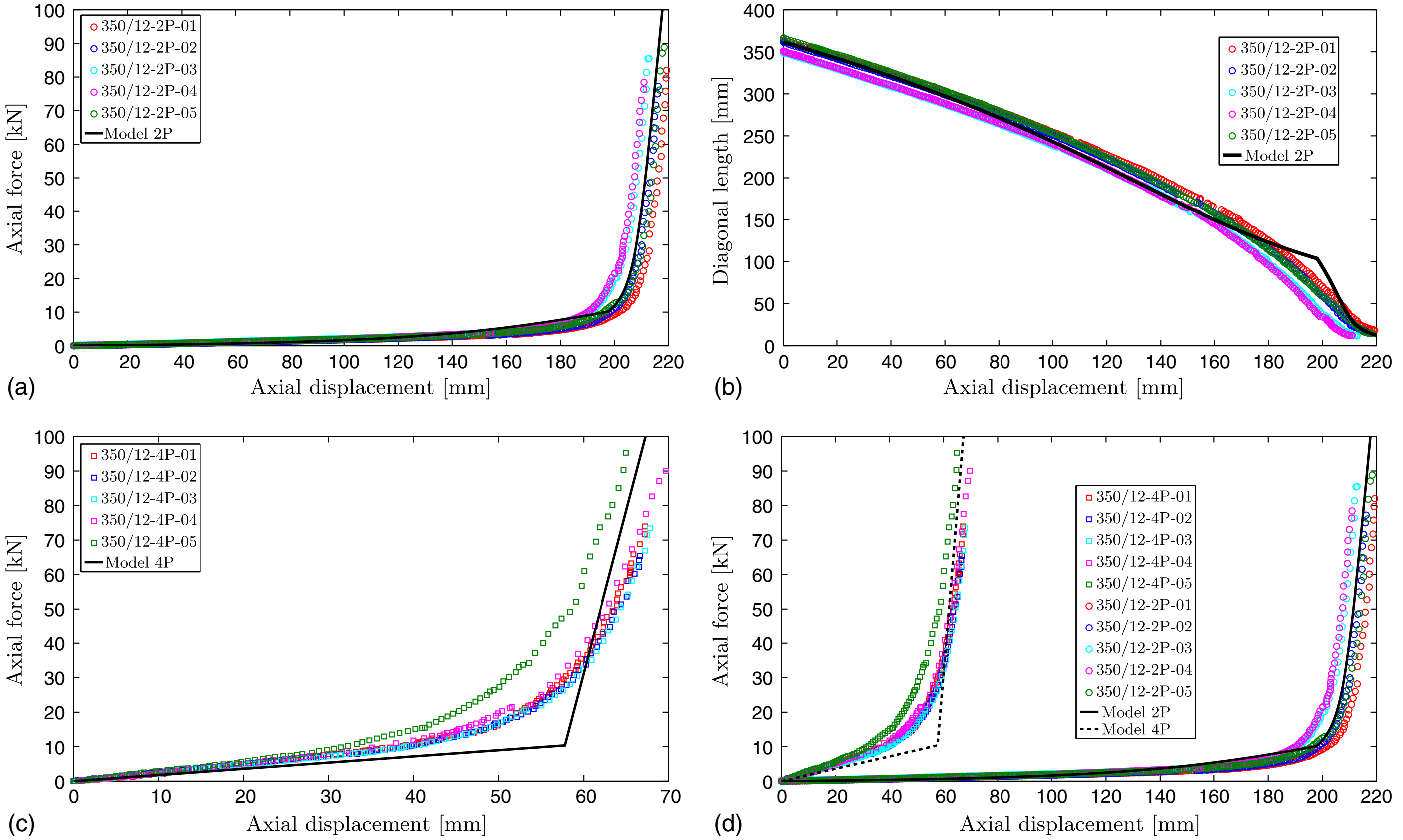

Fig. 7. Monotonic results for 350/12 rings: (a) 2-point traction axial force (calibrated); (b) 2-point traction diagonal length (calibrated); (c) 4-point traction axial force (predicted); (d) 2-point and 4-point traction axial force

in both regimes and both loading configurations because of different modeling choices and stricter geometric assumptions.

Once the optimal parameters from monotonic loading are obtained, the optimal shape-hardening functions are obtained from the unloading cycles. The fitted values of the shape-hardening variables G_p and G_d do increase with deformation [Figs. 8(a and b)], confirming the assumption that the shape-hardening functions are increasing. The assumption that shape-hardening functions g_p and g_d can be taken as power functions is confirmed by the quality of the fit.

As a consequence of the linkages' shape hardening, the force–displacement relationships of the ring exhibit irreversibility over the unloading cycles as shown in Figs. 8(c and d). Only one experimental data set is displayed in order to identify the unloading cycles properly. The stiffness of the springback increases as the axial displacement increases, and the model is able to finely match the unloading cycles of both reference loading cases.

The main results obtained for the 350/09 and 420/16 rings are now presented. For technical reasons, less than five experimental data sets are available in some cases. The overall response of the model for the 350/09 and 420/16 rings is very similar to the one with the 350/12 rings, showing the model generality and adaptability to different sizes of rings.

The 2-point traction force–displacement and diagonal length–displacement curves show good accordance, matching the response of the ring over the bending and tensile regimes (Fig. 9). Similarly, the 4-point traction force–displacement curve presents a satisfying affine response with the same discrepancies in the stiffness that is underestimated in the bending regime and overestimated in the tensile regime. A possible explanation of this difference in the tensile stiffness is that in 4-point traction, the contact angle of the ring on the connecting elements is approximately $\pi/2$ rad (90°), while in 2-point traction it is approximately π rad (180°), the curvature and transverse pressure on the strand is then lower in 4-point traction. As a result, in 4-point traction, sliding between the wires of the spliced ring may be favored and result in a lower tensile stiffness that the model is not able to match because it exhibits identical tensile stiffness in both 2-point and 4-point traction. The unloading cycles in 4-point and 2-point traction also show irreversibility in the deformation and exhibit an increase in the stiffness of the springback because the ring deforms plastically (Fig. 10).

Conclusion

In this paper, an advanced discrete model of steel rings accounting for most physical phenomena is developed. The 2-point and 4-point traction loading configurations are used as references; the analytical response of the ring model under these loading configurations is derived and a multicriteria calibration method to obtain the optimal model parameters is developed based on the Levenberg-Marquardt algorithm. An experimental campaign is conducted for several steel wire spliced rings according to the suggested testing protocol. The model is calibrated against the experimental data from the 2-point traction and shows good agreement. Comparison with the experimental results from the 4-point traction has validated the model capacity to replicate the nonlinear behavior of different rings under different loading configurations.

The formulation of the model makes it more complete than previously existing discrete ring models, and computationally

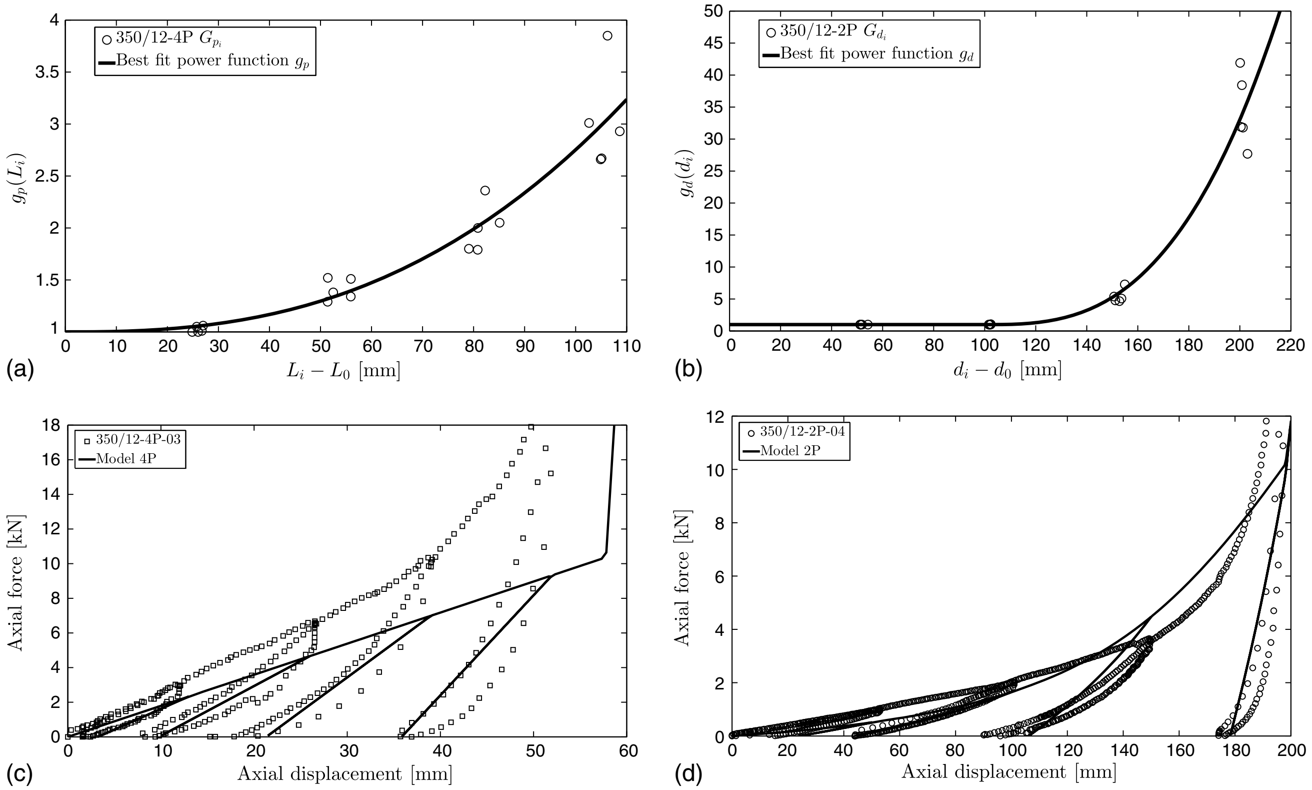

Fig. 8. Unloading results for 350/12 rings: (a) perimeter shape hardening; (b) diagonal shape hardening; (c) 4-point traction axial force; (d) 2-point traction axial force

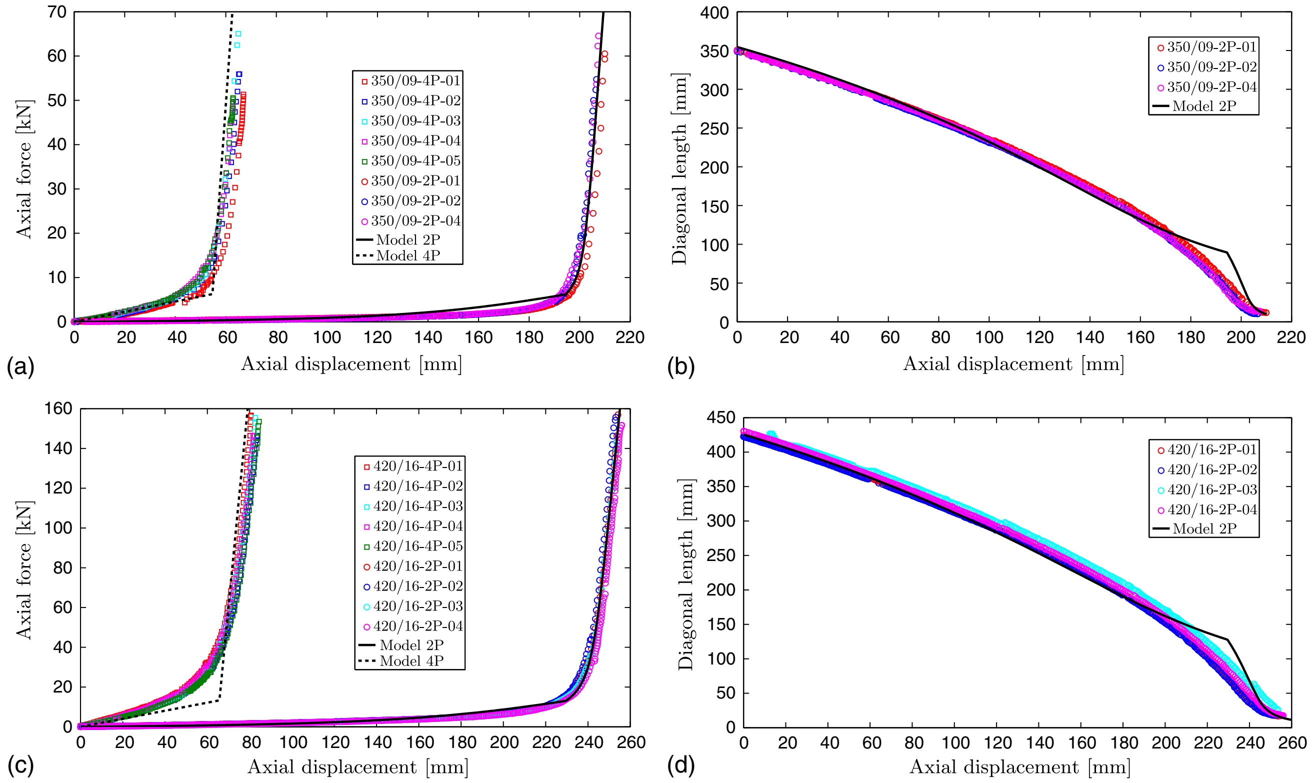

Fig. 9. Monotonic results for 350/09 and 420/16 rings: (a) 350/09 2-point (calibrated) and 4-point (predicted) traction axial force; (b) 350/09 2-point traction diagonal length (calibrated); (c) 420/16 2-point (calibrated) and 4-point (predicted) traction axial force; (d) 420/16 2-point traction diagonal length (calibrated)

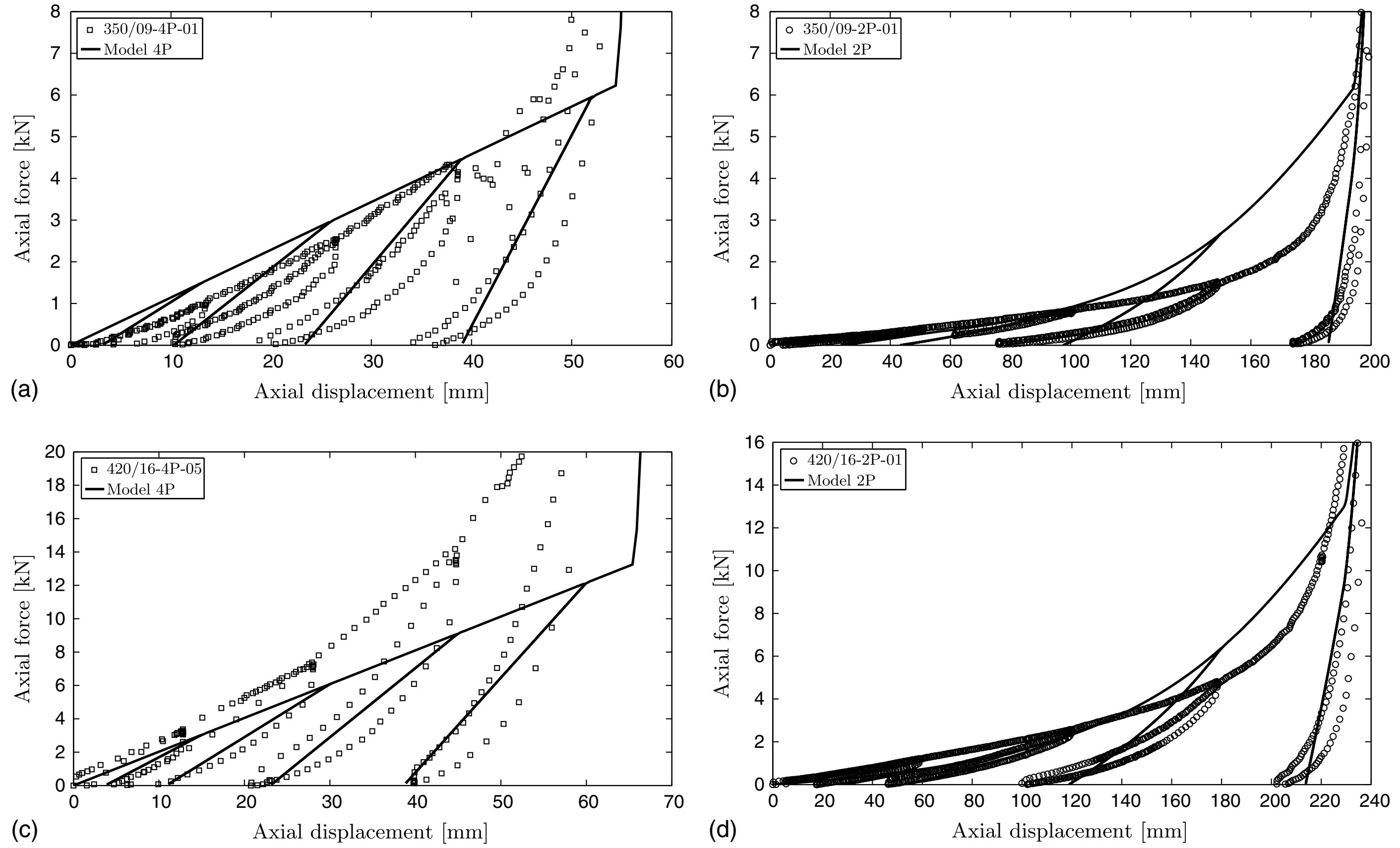

Fig. 10. Unloading results for 350/09 and 420/16 rings: (a) 350/09 4-point traction axial force; (b) 350/09 2-point traction axial force; (c) 420/16 4-point traction axial force; (d) 420/16 2-point traction axial force

inexpensive compared with more exact models while showing good results. Implementations of the model in FEM or DEM codes can be easily derived from the analytical formulation and are assumed to show good computational cost. These features make the present model particularly suitable for the modeling and numerical simulation of large ring net assemblies. The testing protocol and numerical calibration method developed provide effective and robust tools to obtain the model parameters for any given technology of rings. Future developments will be made to assess the membrane behavior of an assembly of rings and investigate the in-plane and out-of-plane response of the net alone and connected to other flexible elements as part of the complete modeling of protection structures.

Appendix I. Demonstrations of the Ring Model Analytical Relationships

This appendix details the demonstrations of Eqs. (11), (13)–(16).

4-Point Traction Unloading Equations

The force–displacement relationship Eq. (11) is now demonstrated. The axial equilibrium equation from [Eq. (9)] is recalled: $F_p + F_{s_1} + F_d \sin\gamma - F/2 = 0$, with $\sin\gamma = (s_0 + \delta)/d$.

The expression of the forces in the linkages during unloading are also recalled: $F_p = 2k_b\delta_i + 2G_{p_i}k_b(\delta - \delta_i)$ for $\delta < \delta_i < \delta_r$, $F_p = 2k_b\delta_r + 2G_{p_r}k_b(\delta - \delta_r)$ for $\delta < \delta_r < \delta_i$, and $F_p = 2k_b\delta_r + 2k_t(\delta - \delta_r)$ for $\delta > \delta_r$, $F_d = G_{d_i}k_d(d - d_i)$, $F_{s_1} = G_{s_i}k_s(\delta - \delta_i)$, and $F_{s_2} = 0$.

The equilibrium equation is then

$$\begin{aligned}
&2k_b\delta_i + 2G_{p_i}k_b(\delta - \delta_i) + G_{s_i}k_s(\delta - \delta_i)\\
&\quad + G_{d_i}k_d(d - d_i)\frac{s_0 + \delta}{d} - \frac{F}{2} = 0 \quad \text{for } \delta < \delta_i < \delta_r\\
&2k_b\delta_r + 2G_{p_r}k_b(\delta - \delta_r) + G_{s_i}k_s(\delta - \delta_i)\\
&\quad + G_{d_i}k_d(d - d_i)\frac{s_0 + \delta}{d} - \frac{F}{2} = 0 \quad \text{for } \delta < \delta_r < \delta_i\\
&2k_b\delta_r + 2k_t(\delta - \delta_r) + G_{s_i}k_s(\delta - \delta_i)\\
&\quad + G_{d_i}k_d(d - d_i)\frac{s_0 + \delta}{d} - \frac{F}{2} = 0 \quad \text{for } \delta_i > \delta > \delta_r
\end{aligned} \tag{24}$$

and can be simply rearranged to obtain Eq. (11).

2-Point Traction Equations

The implicit relations for the axial force F and diagonal length d Eqs. (13)–(16) are now demonstrated. The equilibrium Eq. (12) of the top and side nodes are recalled: $2F_p \sin\gamma + 2F_s \sin\gamma = F - F_{d_1}$ and $2F_p \cos\gamma + 2F_s \cos\gamma = -F_{d_2}$, with $\cos\gamma = [d/(2s)]$ and $\sin\gamma = [(d_0 + \delta)/(2s)]$. Dividing the first equation by the second one yields

$$\tan\gamma = \frac{F - F_{d_1}}{-F_{d_2}} = \frac{d_0 + \delta}{d} \tag{25}$$

Monotonic Loading

The expression of the force in the perimeter linkage is recalled: $F_p = 4k_b(s - s_0)$ for $s < s_r$ and $F_p = 4k_b(s_r - s_0) + 4k_t(s - s_r)$ for $s > s_r$. The axial diagonal and the sides do not develop forces during monotonic loading ($F_s = 0$ and $F_{d_1} = 0$), the force in the transverse diagonal is given by $F_{d_2} = k_d(d - d_0)$, hence Eq. (25) gives

$$\tan\gamma = \frac{F}{k_d(d_0 - d)} = \frac{d_0 + \delta}{d} \tag{26}$$

from which, noting that $d_0 = \phi$, Eq. (14) is directly derived.

The equilibrium equation of the top node is

$$\begin{aligned} 8k_b(s - s_0)\frac{d_0 + \delta}{2s} &= F \quad \text{for } s < s_r \\ [8k_b(s_r - s_0) + 4k_t(s - s_r)]\frac{d_0 + \delta}{2s} &= F \quad \text{for } s > s_r \end{aligned} \tag{27}$$

From which expression of the side length s is directly derived as

$$\begin{aligned} s &= s_0\frac{4k_b(d_0 + \delta)}{4k_b(d_0 + \delta) - F} \quad \text{for } s < s_r \\ s &= \frac{4[k_b(s_r - s_0) - k_t s_r](d_0 + \delta)}{F - 4k_t(d_0 + \delta)} \quad \text{for } s > s_r \end{aligned} \tag{28}$$

Finally, using the Pythagorean trigonometric identity gives an extra equation, $4s^2 = d^2 + (d_0 + \delta)^2$, from which the implicit Eq. (13) is obtained.

Unloading

The expression of the force in the perimeter linkage becomes $F_p = 4k_b(s_i - s_0) + 4G_{p_i}k_b(s - s_i)$ for $s < s_i < s_r$, $F_p = 4k_b(s_r - s_0) + 4G_{p_r}k_b(s - s_r)$ for $s < s_r < s_i$, and $F_p = 4k_b(s_r - s_0) + 4k_t(s - s_r)$ for $s > s_r$. Every internal linkage develops forces during unloading; the expression of these forces are recalled: $F_{d_1} = G_{d_i}k_d(\delta - \delta_i)$, $F_{d_2} = k_d(d - d_0)$, and $F_s = G_{s_i}k_s(s - s_i)$. The demonstration is very similar to the one for the monotonic loading. First, Eq. (25) is written for the given forces

$$\tan\gamma = \frac{F - G_{d_i}k_d(\delta - \delta_i)}{k_d(d_0 - d)} = \frac{d_0 + \delta}{d} \tag{29}$$

from which Eq. (16) is directly derived.

The equilibrium equation of the top node becomes

$$\begin{aligned} &[8k_b(s_i - s_0) + 8G_{p_i}k_b(s - s_i) + 2G_{s_i}k_s(s - s_i)]\frac{d_0 + \delta}{2s} \\ &\quad = F - G_{d_i}k_d(\delta - \delta_i) \quad \text{for } s < s_i < s_r \\ &[8k_b(s_r - s_0) + 8G_{p_r}k_b(s - s_r) + 2G_{s_i}k_s(s - s_i)]\frac{d_0 + \delta}{2s} \\ &\quad = F - G_{d_i}k_d(\delta - \delta_i) \quad \text{for } s < s_r < s_i \\ &[8k_b(s_r - s_0) + 8k_t(s - s_r) + 2G_{s_i}k_s(s - s_i)]\frac{d_0 + \delta}{2s} \\ &\quad = F - G_{d_i}k_d(\delta - \delta_i) \quad \text{for } s_i > s > s_r \end{aligned} \tag{30}$$

From which expression of the side length s is directly derived as

$$\begin{aligned} s &= \frac{[4G_{p_i}k_b s_i + G_{s_i}k_s s_i - 4k_b(s_i - s_0)](\phi + \delta)}{(4G_{p_i}k_b + G_{s_i}k_s)(\phi + \delta) + G_{d_i}k_d(\delta - \delta_i) - F} \quad \text{for } s < s_i < s_r \\ s &= \frac{[4G_{p_r}k_b s_r + G_{s_i}k_s s_i - 4k_b(s_r - s_0)](\phi + \delta)}{(4G_{p_r}k_b + G_{s_i}k_s)(\phi + \delta) + G_{d_i}k_d(\delta - \delta_i) - F} \quad \text{for } s < s_r < s_i \\ s &= \frac{[4k_t s_r + G_{s_i}k_s s_i - 4k_b(s_r - s_0)](\phi + \delta)}{(4k_t + G_{s_i}k_s)(\phi + \delta) + G_{d_i}k_d(\delta - \delta_i) - F} \quad \text{for } s_i > s > s_r \end{aligned} \tag{31}$$

Finally, the implicit Eq. (15) is obtained using the Pythagorean trigonometric identity.

Appendix II. Determination of the Optimal Side Stiffness

This appendix details the demonstration of Eq. (23). Assume that in the 4-contact pattern, the neighboring rings are axially pulled away in opposite directions and are free to move crosswise as shown in Fig. 11(a). Rings will first slide along and meet across the central ring before pulling it in a 2-point traction. The force–displacement relationship for the central ring would first exhibit a zero-force plateau during the initial sliding phase for an axial displacement of the contact points ranging from 0 to $\phi - s_0$. After that initial sliding phase, the force–displacement relationship would be identical to the 2-point traction relationship, shifted by the axial sliding distance $\phi - s_0$. As a consequence, the transition state between the

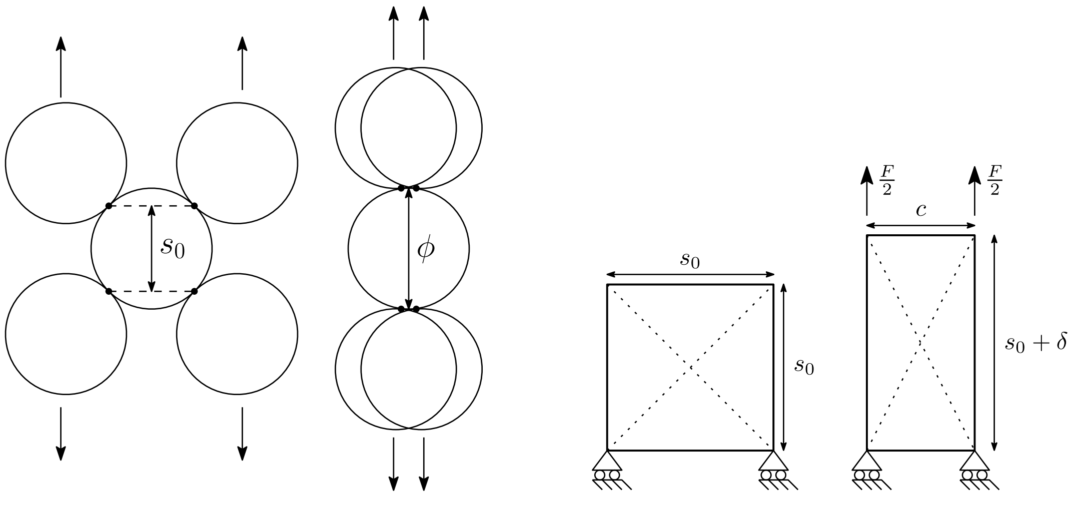

(a)

(b)

Fig. 11. Loading case for the determination of the optimal side stiffness: (a) actual kinematics of the assembly; (b) central ring associated kinematics

bending regime and the tensile regime of the central ring would be reached for a total axial displacement of its contact points of $\phi - s_0 + \delta_r^{2P}$, where δ_r^{2P} denotes the axial displacement at the transition state in 2-point traction [Fig. 4(c)].

The actual sliding of the four contact points along the central ring is modeled by a 4-point traction kinematics without lateral constraint. An axial displacement δ is given to the top nodes, while the bottom nodes are fixed axially, and lateral displacements are permitted [Fig. 11(b)]. The model cannot undergo zero-energy deformations as a result, it is not able to properly reproduce the free sliding of the ring followed by the 2-point traction; nevertheless, the tensile regime of both configurations can be matched. To do so, it is imposed that the transition state for the model is reached for an axial displacement δ_r' equal to the transition axial displacement of the actual configuration, that is

$$\delta_r' = \phi - s_0 + \delta_r^{2P} \tag{32}$$

Narrowing the interest to the transition state allows the study of the model to be limited to monotonic loading in the bending regime. The equilibrium equations of the top nodes are identical to the reference 4-point traction equilibrium Eq. (9), taking away the restraining force ($R = 0$). Diagonal linkages and axial side linkages do not develop compression forces ($F_d = 0$ and $F_{s_1} = 0$) in the bending regime, and equilibrium equations become

$$\begin{aligned} 2k_b(c - s_0 + \delta) &= \frac{F}{2} \\ 2k_b(c - s_0 + \delta) &= k_s(s_0 - c) \end{aligned} \tag{33}$$

The expression of the short side length c as a function of the axial displacement δ is derived from Eq. (33) and is given by

$$c = s_0 - \frac{2k_b}{2k_b + k_s}\delta \tag{34}$$

The transition state is reached when the perimeter length equals the transition perimeter length $L_r = 4s_r$, that is, $2[s_0 + \delta_{r'} + c(\delta_{r'})] = 4s_r$. Using Eqs. (32) and (34), the expression of the optimal side stiffness Eq. (23) is obtained.

Acknowledgments

The authors would like to thank the CAN company for their investment and support in the experimental campaign, providing the rings, testing machine, and sensors. The authors would also like to thank the Vulnérabilité des Ouvrages aux Risques (VOR) research platform for financing the construction of the testing frame. Developments presented in this paper will be part of the French National Project C2ROP (Chute de Blocs, Risques Rocheux et Ouvrages de Protection, www.c2rop.fr).

References

Brent, R. (1973). *Algorithms for minimization without derivatives*, Prentice-Hall, Englewood Cliffs, NJ.

Ehrgott, M. (2005). *Multicriteria optimization*, Springer, Berlin.

EOTA (European Organization for Technical Approvals). (2013). "Guideline for European technical approval of falling rock protection kits." *ETAG 27*, Brussels, Belgium.

Escallón, J., Wendeler, C., Chatzi, E., and Bartelt, P. (2014). "Parameter identification of rockfall protection barrier components through an inverse formulation." *Eng. Struct.*, 77, 1–16.

Gentilini, C., Govoni, L., de Miranda, S., Gottardi, G., and Ubertini, F. (2012). "Three-dimensional numerical modelling of falling rock protection barriers." *Comput. Geotech.*, 44, 58–72.

Ghoussoub, L. (2014). "Analyse de quelques éléments du comportement des écrans de filets pare-blocs." Ph.D. thesis, Univ. Paris-Est, Marne la Vallée, France (in French).

Grassl, H. (2002). "Experimentelle und numerische modellierung des dynamischen tragund verformungsverhaltens von hochflexiblen schutzsystemen gegen steinschlag." Ph.D. thesis, ETH Zurich, Zurich, Switzerland (in German).

Grassl, H., Volkwein, A., Anderheggen, E., and Ammann, J. (2002). "Steelnet rockfall protection—Experimental and numerical simulation." *WIT Trans. Built Environ.*, 63, 11.

Hu, Z., and Zheng, G. (2016). "A combined dynamic analysis method for geometrically nonlinear vibration isolators with elastic rings." *Mech. Sys. Signal Process.*, 76–77, 634–648.

ImageJ version 1.48 [Computer software]. National Institutes of Health, Bethesda, MD.

Lambert, S., and Nicot, F., eds. (2011). *Rockfall engineering*, Wiley, London.

Marquardt, D. W. (1963). "An algorithm for least-squares estimation of nonlinear parameters." *J. Soc. Ind. Appl. Math.*, 11(2), 431–441.

Nicot, F., Cambou, B., and Mazzoleni, G. (2001a). "Design of rockfall restraining nets from a discrete element modelling." *Rock Mech. Rock Eng.*, 34(2), 99–118.

Nicot, F., Cambou, B., and Mazzoleni, G. (2001b). "From a constitutive modelling of metallic rings to the design of rockfall restraining nets." *Int. J. Numer. Anal. Methods Geomech.*, 25(1), 49–70.

Schneider, C., Rasband, W., and Eliceiri, K. (2012). "NIH image to ImageJ: 25 years of image analysis." *Nat. Methods*, 9(7), 671–675.

Seames, A., and Conway, H. (1957). "A numerical procedure for calculating the large deflections of straight and curved beams." *J. Appl. Mech.*, 24, 289–294.

Tse, P., Lai, K., SO, C., and Cheng, C. (1994). "Large deflections of elastic composite circular springs under uniaxial compression." *Int. J. Non Linear Mech.*, 29(5), 781–798.

Tse, P., and Lung, C. (2000). "Large deflections of elastic composite circular springs under uniaxial tension." *Int. J. Non Linear Mech.*, 35(2), 293–307.

Volkwein, A. (2004). "Numerische simulation von flexiblen steinschlagschutzsystemen." Ph.D. thesis, ETH Zurich, Zurich, Switzerland (in German).